Experimental confirmation and physical understanding of ultra-high bit rate impulse radio in the THz digital communication channels of the atmosphere

2014 J. Opt. 16 094004

(http://iopscience.iop.org/2040-8986/16/9/094004)

IOP Publishing Journal of Optics
J. Opt. **16** (2014) 094004 (17pp) doi:10.1088/2040-8978/16/9/094004

INVITED ARTICLE

Experimental confirmation and physical understanding of ultra-high bit rate impulse radio in the THz digital communication channels of the atmosphere

Mahboubeh Mandehgar, Yihong Yang and D Grischkowsky

School of Electrical and Computer Engineering, Oklahoma State University, Stillwater, Oklahoma 74078, USA

E-mail: daniel.grischkowsky@okstate.edu

Received 28 May 2014, revised 15 July 2014
Accepted for publication 25 July 2014
Published 3 September 2014

Abstract

We have performed highly accurate numerical calculations of high bit rate impulse propagation through the seven digital communication channels of the atmosphere at RH 58% ($10\ \mathrm{g\ m^{-3}}$). These calculations maximized bit rates for pathlengths equal to or longer than 100 m. We have experimentally verified our calculations for three channels with a propagation pathlength of 137 m and RH 65% ($11.2\ \mathrm{g\ m^{-3}}$). Excellent agreement between measurement and theory was obtained for **Channel 3** at 252 GHz, bit rate 84 $\mathrm{Gb\ s^{-1}}$, FWHM bandwidth (BW) 180 GHz; **Channel 6** at 672 GHz, 45 $\mathrm{Gb\ s^{-1}}$, BW 84 GHz; and **Channel 7** at 852 GHz, 56.8 $\mathrm{Gb\ s^{-1}}$, BW 108 GHz.

Keywords: THz communications, THz absorption in atmosphere, THz-TDS

(Some figures may appear in colour only in the online journal)

Introduction

In the frequency range from 0.05 to 2 THz, the frequency-dependent absorption of water vapor in the atmosphere $\alpha(\omega)$ and the corresponding dispersive index of refraction $n(\omega)$ control the electromagnetic propagation of broad-bandwidth THz pulses and narrow-band THz waves. Because the index $n(\omega)$ is quite small, the refractivity term $[n(\omega)-1]$ is usually discussed. The strong absorption by water vapor determines the maximum propagation distance of THz waves in the atmosphere, while the reshaping of propagating broad-bandwidth short THz pulses is controlled by both the refractivity and the absorption. Many simulation codes have been developed to model the absorption of THz radiation by water vapor in the atmosphere [1–4]. Of most interest for applications are the regions (windows) of relative transparency between the absorption resonance peaks. The early high quality investigations into the propagation of near-millimeter waves from 100 GHz to 1000 GHz within the water windows is well described in [1], which includes both theoretical and experimental investigations. More recent overviews are given in Refs. [3] and [4]. Recently, there has been a precise THz-TDS characterization of water vapor from 0.2 to 2.0 THz [5]. These THz pulse propagation measurements [5] provided the complex THz pulse transmission data to test a powerful simulation approach [6] based on the complete van Vleck-–Weisskopf lineshapes for both $\alpha(\omega)$ and $[n(\omega)-1]$ [7, 8], summed over either the JPL or the HITRAN databases [9, 10]. Excellent agreement was obtained [6].

THz wireless communication has the potential to have an impact on important network problems, and this potential has been discussed in recent reviews [11–16]. Important problems for the operating worldwide telecommunications network include providing isolated cities, islands, communities, and remote industrial, technical and scientific sites with wideband access to the fiber backbone. Two further longstanding problems include the ability to provide emergency, high-bandwidth backup service in case of loss of an optical fiber link, as well as to provide sports stadiums, shopping malls and older large office buildings in cities with full high bandwidth services.

Using the powerful database simulation approach [6], the potential of the THz digital communication channels of two of the most promising water windows has been discussed [17]. Most recently, the seven water vapor windows in the atmosphere from 60 GHz to 1000 GHz have been characterized at RH 58% and 20 °C (density of $10\,\mathrm{g\,m^{-3}}$) [18], as shown in figure 1. This characterization also includes the oxygen resonance lines and the continuum absorption [19], is considered to be quite accurate and is consistent with previous calculations and measurements [3–5]. The digital communication channels shown in figure 1 were previously analyzed for a channel absorption loss of 10 dB. The optimal bandwidth, center frequency and consequent bit rate were determined from the loss-limited propagation properties for a distance with 10 dB loss [18].

However, for many applications including Internet data centers and high-performance computing systems [20], the highest bit rate possible is desired, and much reduced propagation distances are acceptable. Recently, there have been several demonstrations of THz high bit rate digital communication links of very short lengths [21–26]: $2.5\,\mathrm{Gb\,s^{-1}}$ error-free links at 625 GHz for several meters [21], $25\,\mathrm{Gb\,s^{-1}}$ MMIC-based link at 220 GHz for 10 m [22], and $24\,\mathrm{Gb\,s^{-1}}$ link at 300 GHz for 0.5 m [23]. Most recently, combining THz wireless with photonics technologies, a 20 m direct digital link at 237.5 GHz with a bit rate of $100\,\mathrm{Gb\,s^{-1}}$ has been reported [24]. Demonstrations were made of error-free transmission with a carrier at 300 GHz of $40\,\mathrm{Gb\,s^{-1}}$ for a single channel and $48\,\mathrm{Gb\,s^{-1}}$ for polarization multiplexing for 0.5–1.0 m [25], and a hybrid (photonic Tx and electronic Rx) THz communication system with a carrier at 400 GHz. A bit rate of $40\,\mathrm{Gb\,s^{-1}}$ for 2 m [26] has been presented.

Here, we present new impulse radio [27–30], wide-band, high bit rate, dispersion-limited THz impulse propagation simulations for these seven channels with the emphasis on the highest possible bit rates. In addition, for the first time we provide 137 m THz-TDS experimental confirmation of our impulse propagation simulations for three of the highest bit rate channels.

Numerical simulations—theory and discussion

This paper concentrates on determining the maximum bit rates with simple impulse radio for each of the seven communication channels. This will be done using fundamental linear response theory calculations based on the characterization of figure 1 [18]. For the maximum bit rate, the corresponding propagation distance is limited by impulse broadening and not by absorption. For the Channels 3, 6 and 7, the calculations are compared with the corresponding measurements and achieve excellent agreement, thereby demonstrating the accuracy of the calculations, based on summing over the HITRAN databases for water vapor and oxygen. The broadening of the propagating impulse is mainly due to the frequency-dependent dispersion of the refractivity of water vapor and oxygen. In the frequency domain, if we designate the phase of the THz wave as $\Phi(\omega,z) = \beta(\omega)z$, we can expand beta $\beta(\omega)$ in a Taylor series about the carrier angular frequency ω_c as [31],

$$\begin{aligned}\beta(\omega) = {} & \beta(\omega_c) + \left(\frac{\partial\beta}{\partial\omega}\right)_{\omega_c}(\omega-\omega_c)\\ & + \frac{1}{2}\left(\frac{\partial^2\beta}{\partial\omega^2}\right)_{\omega_c}(\omega-\omega_c)^2\\ & + \frac{1}{3!}\left(\frac{\partial^3\beta}{\partial\omega^3}\right)_{\omega_c}(\omega-\omega_c)^3 + \ldots \qquad (1)\end{aligned}$$

Equation (1) is then rewritten in the simpler notation as

$$\begin{aligned}\beta(\omega) = {} & \beta(\omega_c) + \beta_1(\Delta\omega) + \frac{1}{2}\beta_2(\Delta\omega)^2\\ & + \frac{1}{3!}\beta_3(\Delta\omega)^3 + \frac{1}{n!}\beta_n(\Delta\omega)^n. \qquad (2)\end{aligned}$$

In equation (2) the terms $\beta(\omega_c)$ and β_1 are responsible for pulse propagation with the group velocity, and these terms do not reshape the propagating pulse. The terms β_2, and β_3 and higher terms are responsible for the pulse broadening and reshaping. The seven highlighted bands are located in regions of relatively small and stable GVD, as shown in figures 1(c) and 2(b). The importance of β_2, the group velocity dispersion (GVD) term, can be shown by calculating the magnitude of the phase modulation/km for Channel 3, using the relationship $\Delta\Phi = 0.5\ \beta_2\ (\Delta\omega)^2z$. As shown in figure 2(a), with respect to Channel 3 with the carrier frequency of 252 GHz, the increasing phase shift can be fit with a linearly increasing phase shift due to β_1, which does not broaden the THz pulse, and a $\Delta\Phi = 0.5\ \beta_2\ (\Delta\omega)^2z$ term, which broadens and reshapes the pulse. From figure 2(b), β_2 is approximately $30\,\mathrm{ps^2\,km^{-1}}$ at the 252 GHz carrier frequency of Channel 3. Evaluating $\Delta\Phi = 0.5\ \beta_2\ (\Delta\omega)^2z$, with $\Delta\omega = 2\pi\ 50\,\mathrm{ns}$ (corresponding to 50 GHz) and $z = 1\,\mathrm{km}$, we obtain the value of $\Delta\Phi = 1.5$ radians, in good agreement with figure 2(a). As shown by this example, β_2 (shown in figures 1(c) and 2(b)) is a good parameter to describe the severity of pulse broadening, even though our calculations, as shown in equation (3), use the precisely calculated phase angle. In contrast, the optical case uses the pulse envelope of the slowly varying wave approximation [31], which includes β_2 as a parameter.

For our simulation calculations we use the full linear dispersion theory calculation as described below. The propagated THz impulses are obtained from the linear dispersion theory calculation in the frequency domain [6], using the absorption and phase displayed in figure 1, as shown below.

$$\mathrm{E}(z,\omega) = \mathrm{E}(0,\omega)\exp\left[i\Delta k(\omega)z\right]\exp\left[-\alpha(\omega)z/2\right] \qquad (3)$$

for which the input complex amplitude spectrum is given by

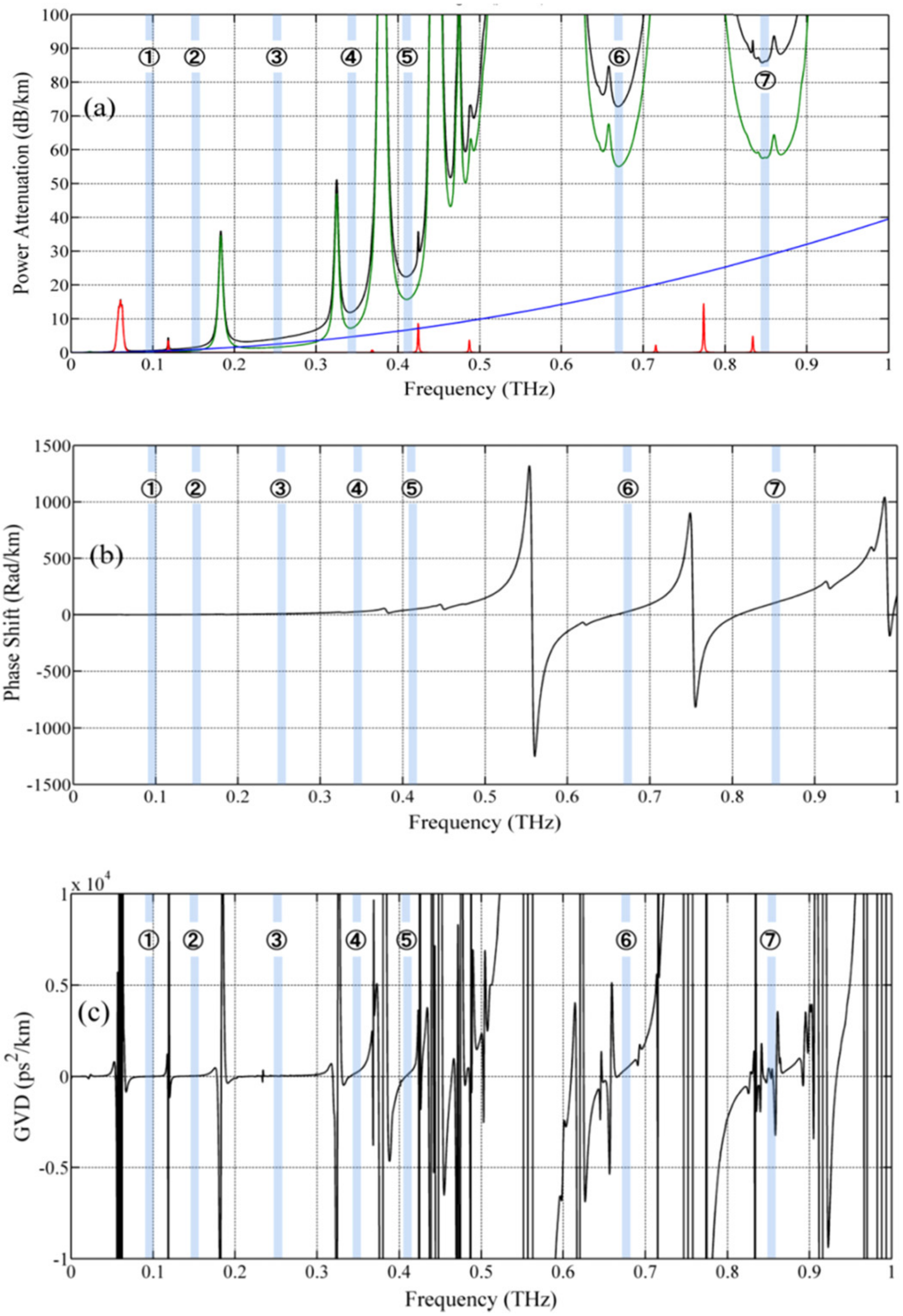

Figure 1. Summary results for the atmosphere at RH 58% and 20 °C (density of 10 g m^{-3}). Reprinted with permission from [18]. Copyright 2014 Springer. The numbered shaded lines mark the digital communication channels at 96 GHz, 144 GHz, 252 GHz, 342 GHz, 408 GHz, 672 GHz, and 852 GHz. (a) The MRT + the continuum absorption + oxygen absorption is shown as the upper black curve in units of dB/km. The MRT absorption [19] is shown as the lower green curve. The continuum absorption is shown as the lowest blue curve. The oxygen absorption lines are shown as the lowest (red) resonance lines. (b) The vV-W-HITRAN + oxygen phase in units of Radians/km. (c) The corresponding group velocity dispersion (GVD) in units of (ps^2/km).

E(0, ω), and the output complex spectrum is given by E(z, ω). The phase is $\Phi = \Delta k(\omega) z$; note that $\Delta k(\omega) = \beta(\omega)$. The amplitude transmission is $\exp[-\alpha(\omega) z/2]$. The wave vector $\Delta k(\omega)$ and the absorption coefficient $\alpha(\omega)$, are based on the complete van Vleck–Weisskopf lineshapes [7, 8] summed over either the JPL or the HITRAN databases [9, 10]. The resulting time-domain pulses are the IFFT of E(z, ω) of equation (3).

The following figures 3–12 show THz impulse bit-pulse propagation calculations for six bit slots containing three transform-limited THz ‘one’ bit, return-to-zero impulses

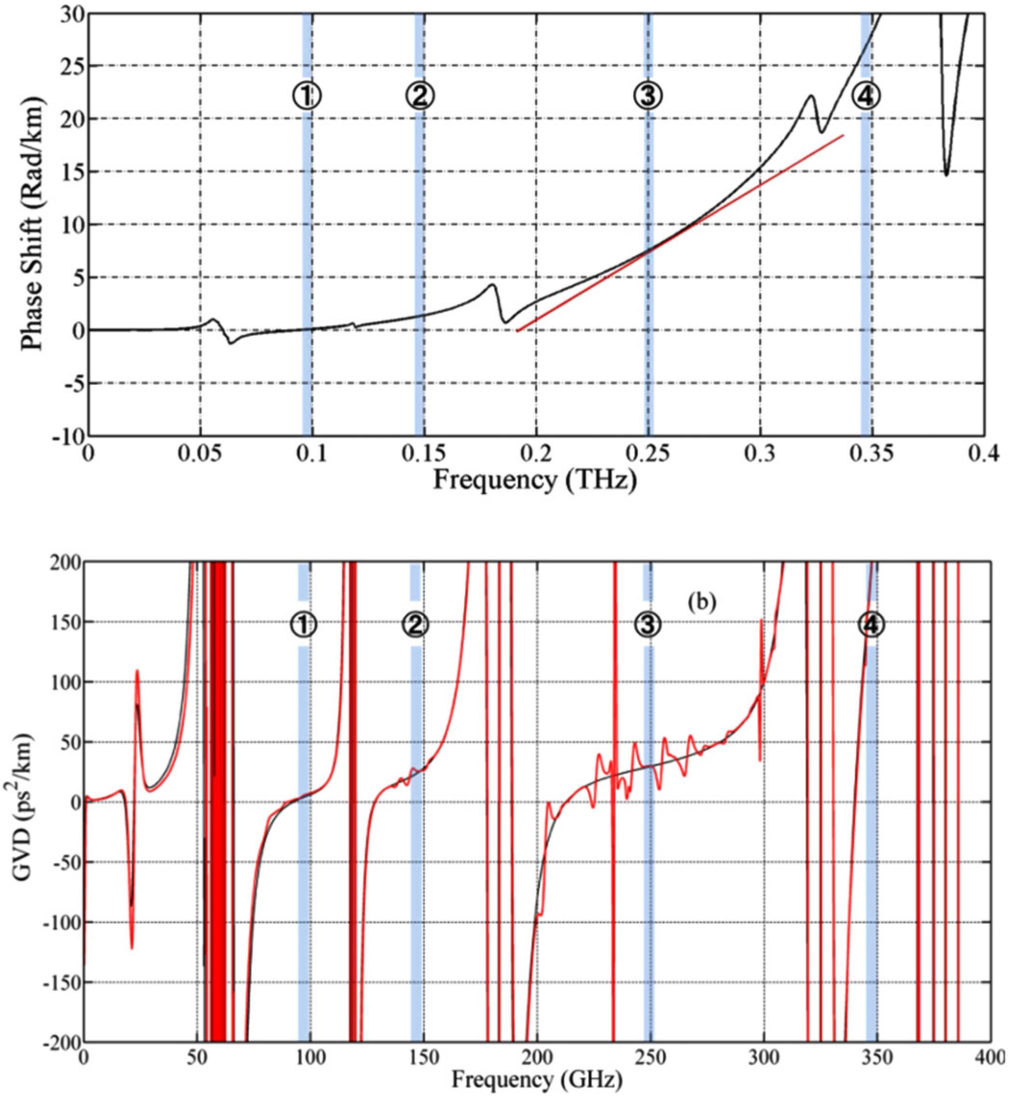

Figure 2. The numbered shaded lines mark the digital communication channels at 96 GHz, 144 GHz, 252 GHz, and 342 GHz. (a) Calculated vV-W-HITRAN phase Φ in radians for a 1 km length of water vapor at RH 58% (10 g m^{-3}) and 20 °C and O_2 vapor in the atmosphere. (b) GVD in ps^2/km from the phase results of figures 1(b) and 2(a). GVD = 2.44 ps^2 km^{-1} at 96 GHz, GVD = 21.6 at 144 GHz, GVD = 29.7 at 250 GHz, and GVD = 55.2 at 342 GHz.

comprising the bit sequence of (011 010), before and after passage through the atmosphere with RH 57.8% (10 g m^{-3}) and 20 °C for a pathlength limited by the pulse broadening. The coherent bits are separated by an integral number of cycles of the center (carrier) frequency, which determines the bit rate, and consequently, the maximum possible bit rate corresponds to only one cycle of the carrier. The symmetry of the input impulses shows that they are transform-limited with their envelopes determined by the ideal raised-cosine amplitude spectrum [31], centered on the indicated carrier frequency. Their corresponding FWHM bandwidths (BW) are also indicated. These coherent bit pulses are changed to current pulses by simulating homodyne detection with the local oscillator (LO) frequency equal to the carrier frequency and with a power detector. The calculated current bit pulses were obtained from the homodyne low frequency component centered on zero frequency.

The resulting ‘one’ bit current pulses are ideal for digital electronics, as shown by their well resolved (011 010) bit sequence, for which the six vertical lines mark the decision-point bit centers of the bit slots. From an inspection of the propagation results, high bit rates are obtained with the initial FWHM of the homodyne pulsewidths of the order of one-half of the bit slot. For all of the channels, the propagated bits are well resolved and are indicated by the circles at the decision-point centers of the bit slots, providing a good binary separation between ones and zeros.

The maximum bit rate distance product for the results is the largest product that still enables good synchronization between the bit rate clock (integer number of cycles of LO) indicated by the six vertical lines in the simulation figures, as well as provides an acceptable signal difference between the ones and zeros. In a real system, the maximum bit rate would be determined by the allowable bit error rate, determined by the system noise on the ones and zeros and the signal

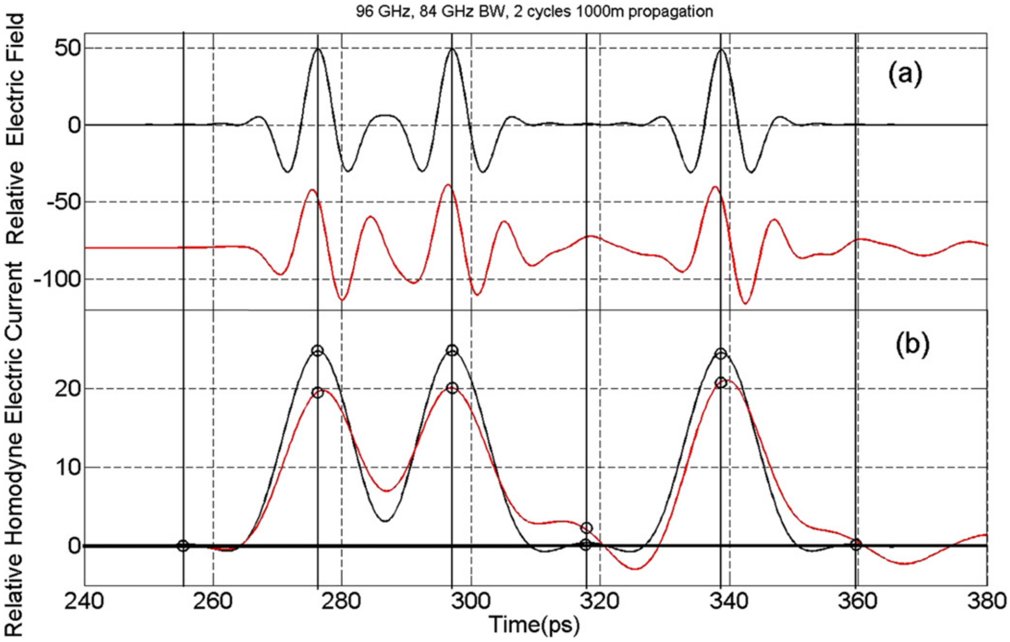

Figure 3. Channel 1. (a) 96 GHz, 48.0 Gb s^{-1}, (2 cycles), 84 GHz BW, input THz 'one' bit impulses (black larger pulses) and calculated smaller, red output impulses after 1 km propagation in the atmosphere with RH 58% (10 g m^{-3}) and 20 °C. (b) Calculated homodyne input upper black current pulses and the output lower red pulses, clearly showing the (011 010) bit sequence, marked by the solid vertical lines. Decision-point values are marked by the black circles.

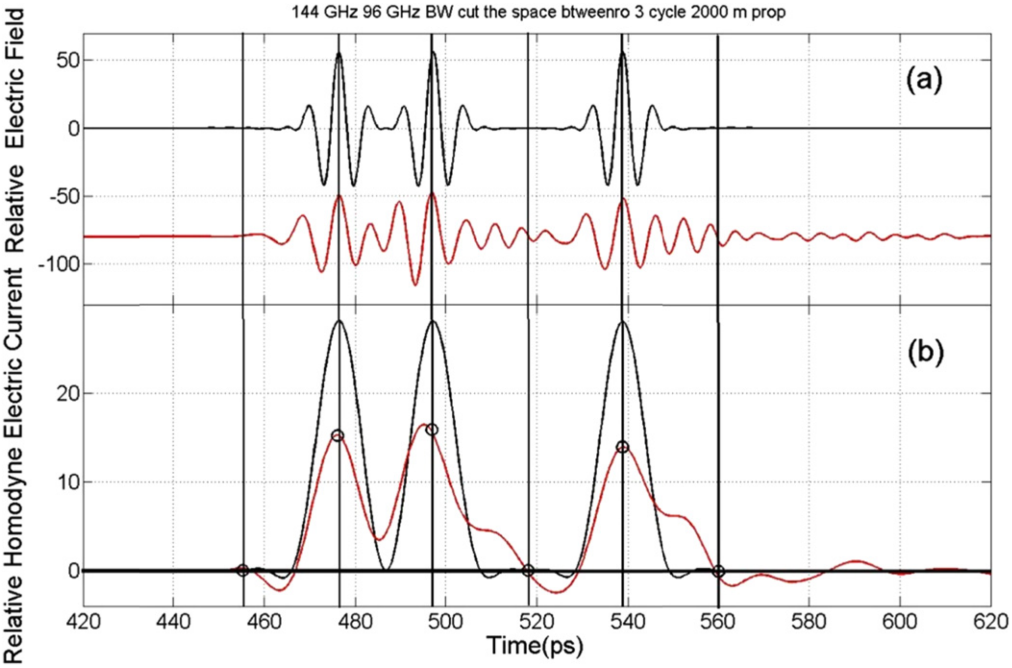

Figure 4. Channel 2. (a) 144 GHz, 48.0 Gb s^{-1}, (3 cycles), 96 GHz BW, input THz 'one' bit impulses (black larger pulses) and calculated smaller, red output impulses after 2 km propagation in the atmosphere with RH 58% (10 g m^{-3}) and 20 °C. (b) Calculated homodyne input upper black current pulses and the output lower red pulses, clearly showing the marked (011 010) bit sequence. Decision-point values are marked by the black circles.

difference between them, as would be shown in the 'eye-diagram'. Here, we don't have capability to do this. However, from our study of the first complete set of simulations, we obtain the intuitive empirical criteria that the maximum product occurs when the signal dip (corresponding to the return to zero of the impulses) between the decision points of the two adjacent homodyne pulses disappears, with respect to the line connecting the two decision points. This disappearance indicates a merging of the two, one-bit pulses. This limit is almost reached only for Channel 6, as shown in figure 10. For the other Channels 1–5 and 7, either the propagation distance

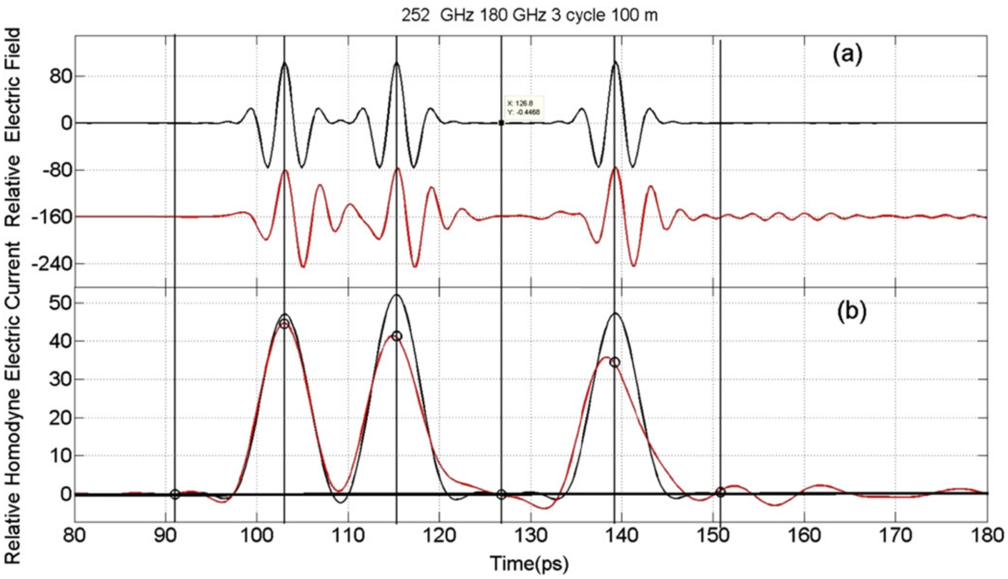

Figure 5. Channel 3. (a) 252 GHz, 84.0 Gb s^{-1}, (3 cycles), 180 GHz BW, input THz 'one' bit impulses (black larger pulses) and calculated smaller, red output impulses after 100 m propagation in the atmosphere with RH 58% (10 g m^{-3}) and 20 °C. (b) Calculated homodyne input upper black current pulses and the output lower red pulses, clearly showing the marked (011 010) bit sequence. Decision-point values are marked by the black circles.

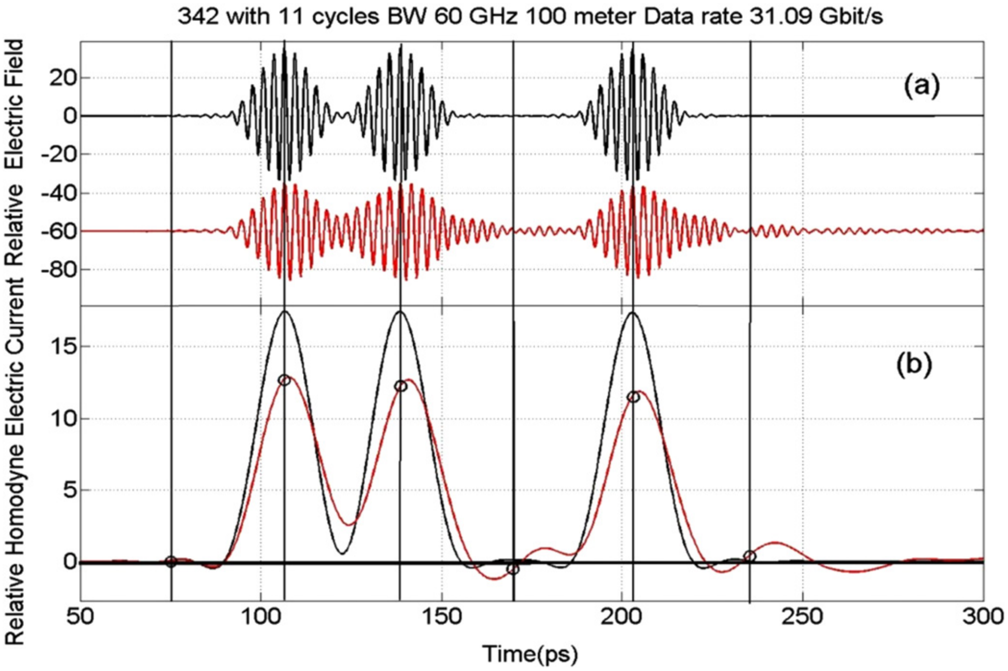

Figure 6. Channel 4. (a) 342 GHz, 31.1 Gb s^{-1}, (11 cycles), 60 GHz BW, input THz 'one' bit impulses (black larger pulses) and calculated smaller, red output impulses after 100 m propagation in the atmosphere with RH 58% (10 g m^{-3}) and 20 °C. (b) Calculated homodyne input upper black current pulses and the output lower red pulses, clearly showing the marked (011 010) bit sequence. Decision-point values are marked by the black circles.

could be increased and/or the number of cycles could be reduced, to more closely approach this limit.

As an example of the approach to this limit, consider Channel 5 at 408 GHz as shown in figure 7 with the bit rate product of (31.4 Gb s^{-1})(0.110 km), and the well-defined 50% signal dip highlighted in yellow. Now, figure 8 shows the monotonic changes with propagation length for Channel 5, for the calculated impulses and homodyne current pulses with the doubled propagation distance of 220 m. The two impulses have merged more closely together with the zero bit in front of the third impulse remaining clearly observable. The corresponding homodyne data pulses still show a very small dip between the two one bit pulses. Figure 9 shows the calculated impulses and homodyne current pulses for the propagation distance again doubled to 440 m. Now the two impulses have merged together, and the zero bit before the third impulse is

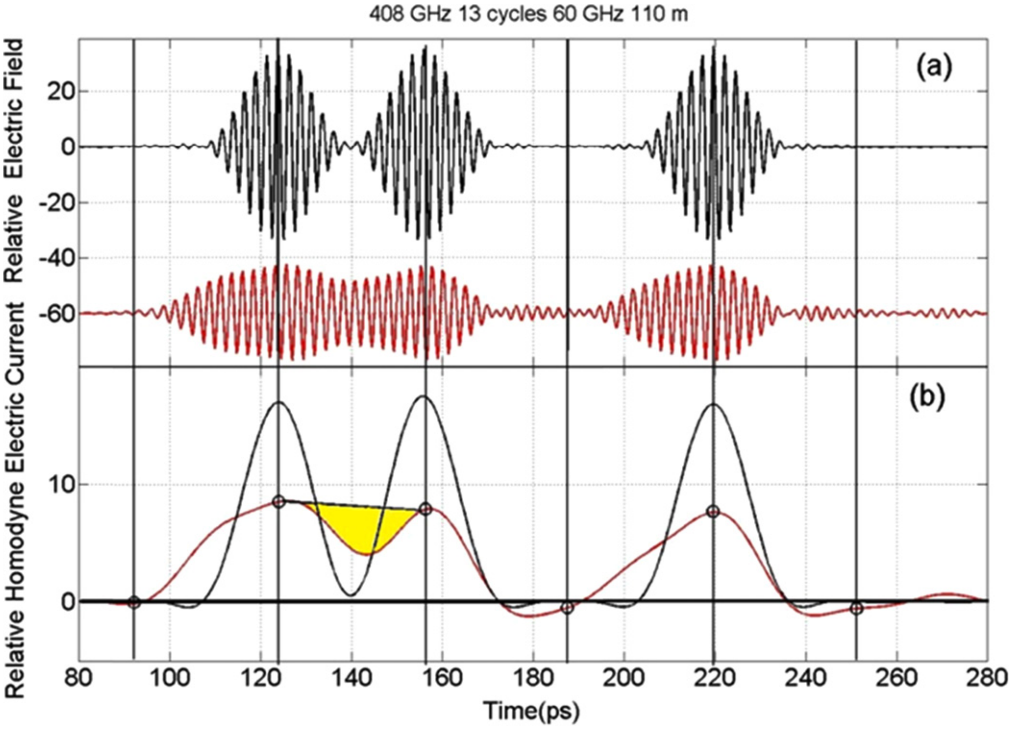

Figure 7. Channel 5. (a) 408 GHz, 31.4 Gb s^{-1}, (13 cycles), 60 GHz BW, input THz 'one' bit impulses (black larger pulses) and calculated smaller, red output impulses after 110 m propagation in the atmosphere with RH 58% (10 g m^{-3}) and 20 °C. (b) Calculated homodyne input upper black current pulses and the output lower red pulses, clearly showing the marked (011 010) bit sequence. Decision-point values are marked by the black circles. The 50% dip of the propagated homodyne signal between the two adjacent 1 bits is highlighted in yellow.

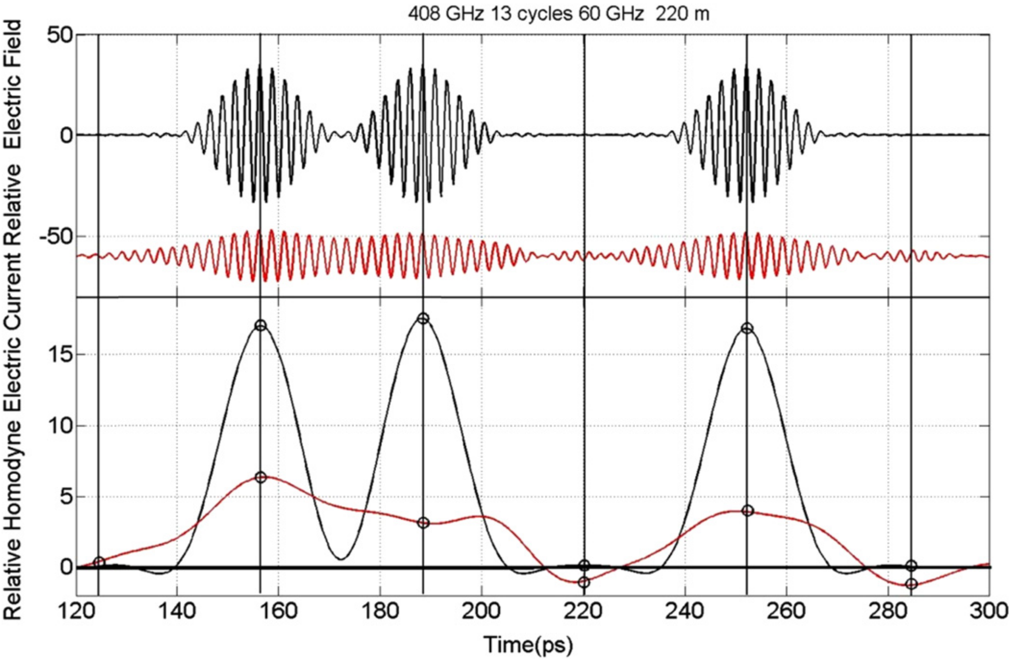

Figure 8. Channel 5. 408 GHz, 31.4 Gb s^{-1}, (13 cycles), 60 GHz BW. Same conditions as figure 7, but with the propagation distance increased to 220 m.

still clearly observable. The corresponding homodyne data pulses no longer show the signal dip between the two one bit pulses, indicating the merging of these pulses. However, the bit sequence is still clearly observable. According to the limit condition, this should be the maximum bit rate product of (31.4 Gb s^{-1})(0.440 km).

As an example of the other approach to the maximum bit rate distance product, consider Channel 7 at 852 GHz, as shown

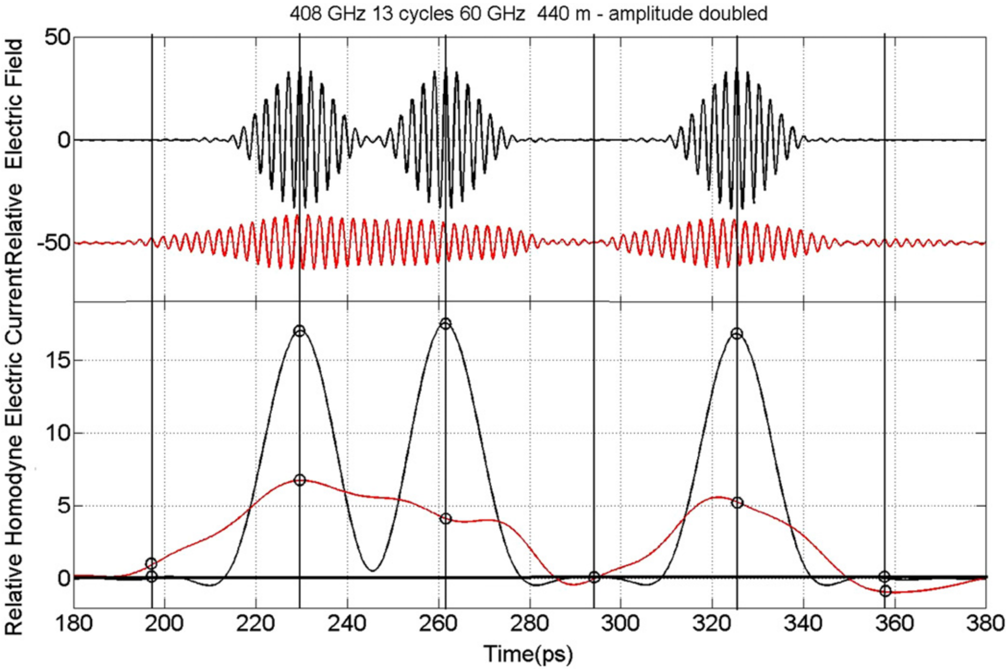

Figure 9. Channel 5. 408 GHz, 31.4 Gb s^{-1}, (13 cycles), 60 GHz BW. Same conditions as figure 7, but with the propagation distance increased to 440 m.

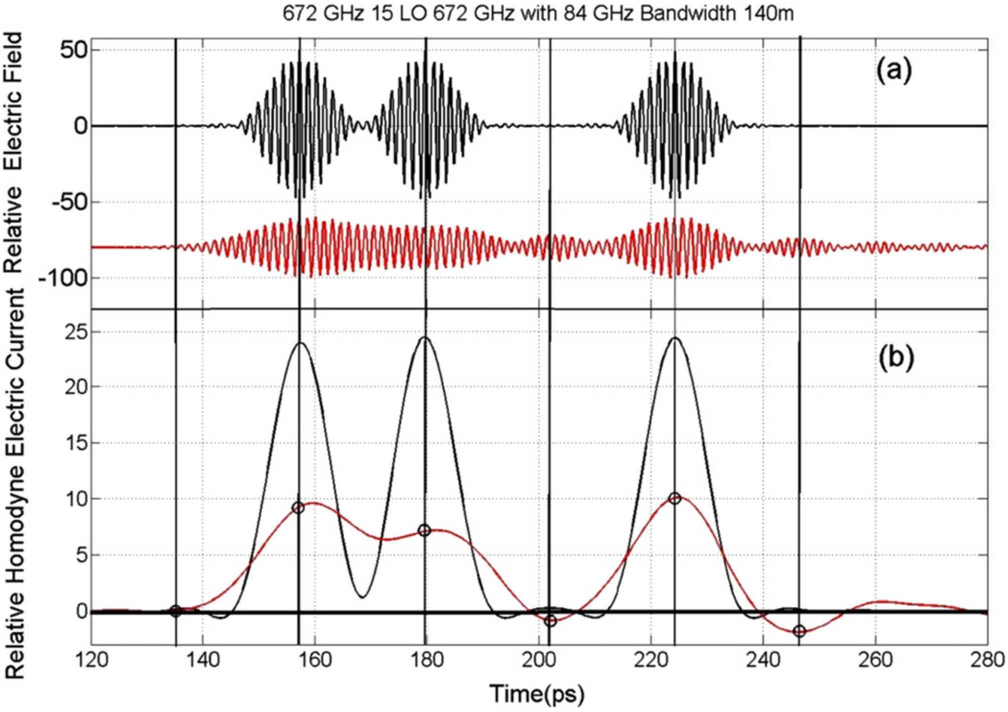

Figure 10. Channel 6. (a) 672 GHz, 44.8 Gb s^{-1}, (15 cycles) 84 GHz BW, input THz 'one' bit impulses (black larger pulses) and calculated smaller, red (multiplied by 2) output impulses after 140 m propagation in the atmosphere with RH 58% (10 g m^{-3}) and 20 °C. (b) Calculated homodyne input upper black current pulses and the output lower red (multiplied by 2) pulses, clearly showing the marked (011 010) bit sequence. Decision-point values are marked by the black circles.

in figure 11, with the bit rate distance product of (56.8 Gb s^{-1}) (0.120 km), and the well-defined 40% signal dip highlighted in yellow. For this example, the bit rate is increased by decreasing the impulse separation to 12 cycles of the carrier, corresponding to a bit separation of 14.08 ps, and the resulting bit rate of 71.0 Gb s^{-1}. Now the corresponding increase in the bit rate distance product to (71.0 Gb s^{-1})(0.100 km) is shown in figure 12. Again, the two impulses have merged more closely together with the zero bit before the third impulse remaining clearly observable. The corresponding homodyne data pulses

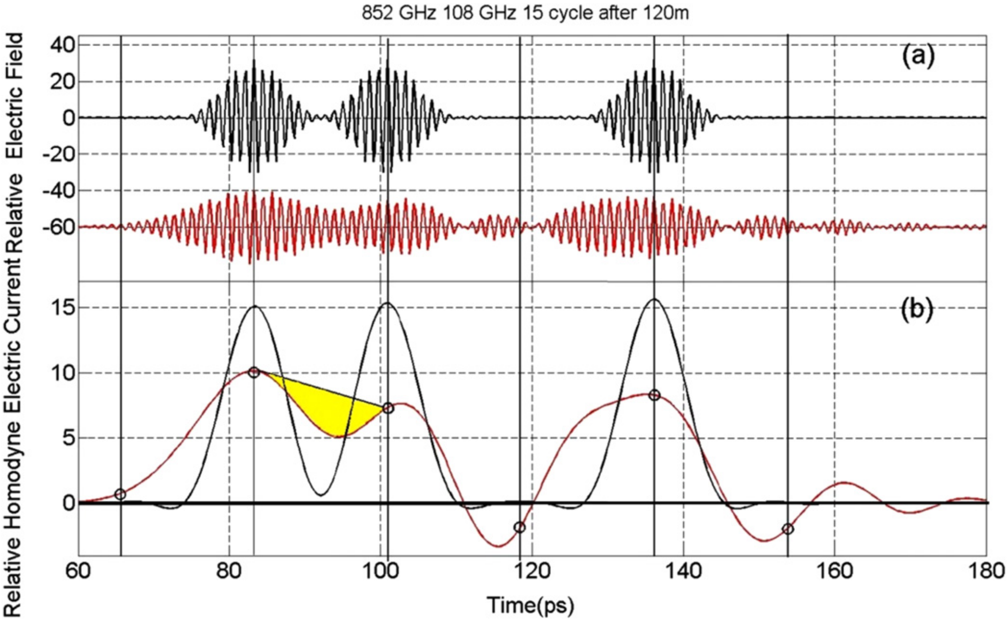

Figure 11. Channel 7. (a) 852 GHz, 56.8 Gb s^{-1}, (15 cycles), 108 GHz BW, input THz 'one' bit impulses (black larger pulses) and calculated smaller, red (multiplied by 2) output impulses after 120 m propagation in the atmosphere with RH 58% (10 g m^{-3}) and 20 °C. (b) Calculated homodyne input upper black current pulses and the output lower red (multiplied by 2) pulses, clearly showing the marked (011 010) bit sequence. Decision-point values are marked by the black circles. The 40% dip of the propagated homodyne signal between the two adjacent 1 bits is highlighted in yellow.

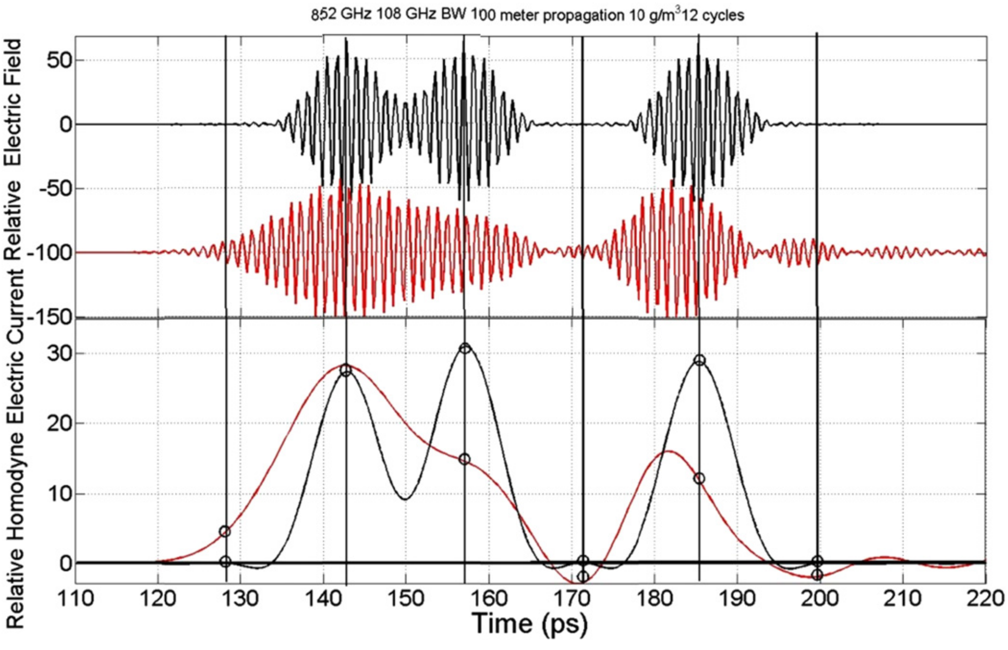

Figure 12. Channel 7. (a) 852 GHz, 108 GHz BW. Same conditions as figure 9, but with the bit rate increased to 71.0 Gb s^{-1}, (12 cycles), and the propagation distance of 100 m.

still show a very small dip between the two one bit pulses, indicating a close approach to the maximum value.

Impulse radio

Impulse radio is a radio technology pioneered by R. A. Scholtz [27] and others [28]. The difference between impulse radio and conventional radio transmissions is that while conventional systems transmit information by varying the power level, frequency, and/or phase of a sinusoidal wave, impulse radio transmits information by generating impulses at specific time intervals, thus enabling pulse position or time modulation. Information can also be modulated on the impulses by encoding the polarity of the impulse or its amplitude, and/or by using orthogonal impulses.

It is important to point out that the large bandwidth associated with the impulse radio impulses usually completely covers the communication channel, in contrast to standard amplitude modulation (ASK) which has a well-defined carrier, and for which the bandwidth is much smaller than the carrier frequency. For impulse radio, the corresponding power spectral density is quite low, and thereby, impulse radio can share the spectrum without affecting more conventional transmission with much narrower bandwidths and much higher power densities. Similar to spread spectrum techniques, impulse radio communications transmit in a manner that does not interfere with conventional narrowband and carrier waves used in the same frequency band. Because of these features, the FCC and the International Telecommunication Union Radio-communication Sector (ITU-R) currently refer to impulse radio as ultra-wideband technology (UWB).

One performance measure of a radio in communication applications is the channel capacity for a given bandwidth and signaling format. According to the Shannon–Hartley theorem, the channel capacity of a properly encoded signal is proportional to the bandwidth of the channel and to the logarithm of the power signal-to-noise ratio (SNR), assuming additive white Gaussian noise. Thus, channel capacity increases linearly with bandwidth to the maximum value available, or (with fixed-channel bandwidth) by increasing the signal power exponentially, and thereby increasing the SNR exponentially. By virtue of the large bandwidths of impulse radio systems, large channel capacities can be achieved, (given sufficient SNR) without using the complex higher-order phase modulations requiring very high SNR. Using forward error correction, high-data-rate impulse radio systems can provide channel performance approaching the Shannon limit.

In this paper, we simulate and experimentally verify coherent homodyne detection of impulse digital data. In principle, the homodyne detection SNR is 3 dB more than for heterodyne detection [31], and for phase modulated digital data (phase-shift-keying, PSK) with the same bit rate, the SNR is 6 dB more than for amplitude modulation (amplitude-shift keying, ASK), for both homodyne and heterodyne detection. In addition PSK eliminates nonlinear propagation effects.

Numerical simulation results

The simulations are summarized in the following table 1, which shows the achievable bit rates and other properties of the 7 THz communication channels of the atmosphere. From an inspection of the table, these links have excellent bit rates using simple amplitude modulation (amplitude shift keying).

Experimental confirmations

We will now briefly describe our experimental measurements that enable direct comparison with the calculated bit sequence. As shown in figure 13, our 170 m long-path THz-TDS system includes a 137 m path in the RH-controlled sample chamber, outlined in red. This system has previously been described in detail [32, 33]. The transit time of THz impulses propagated through the long-path is measured to a precision of 0.1 ps by the THz-TDS transceiver, using the mode-locked laser as an optical clock. The transit time has been shown to have a linear relation with the RH (water vapor density) inside the RH-controlled sample chamber [33].

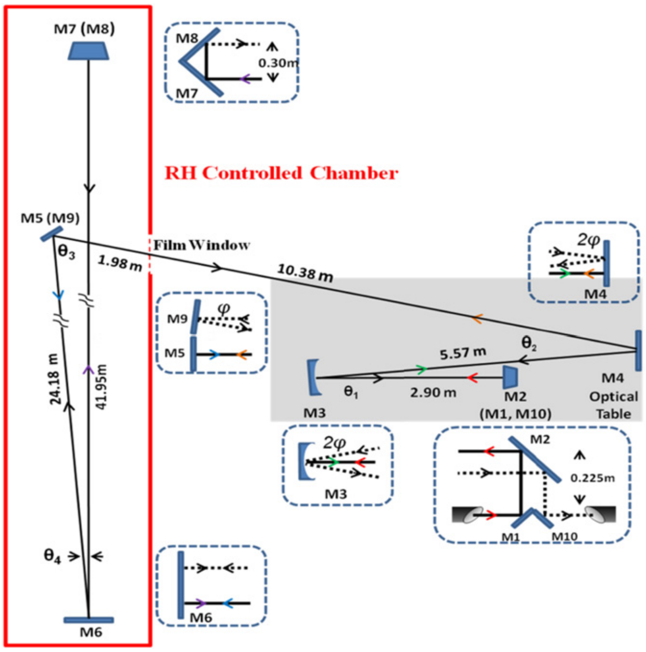

Figure 13. Experimental set up with 170 m long-path system.

The experimental measurements of a transmitted reference impulse with RH 8% and a transmitted impulse with RH 65% are shown in figure 14(a), and their corresponding amplitude spectra are shown in figure 14(b). Using our linear dispersion theory simulation program, it was possible to back-propagate the RH 8% impulse to check for consistency and to determine the phase modulated input spectrum with no water lines. The back-propagation was stopped when the absorption lines with RH 8% disappeared. The corresponding phase modulated input spectrum is shown as the upper line in figure 14(b), and the corresponding asymmetric input impulse (calculated by IFFT) as the blue upper pulse in figure 14(a).

Given this complex input spectrum, it is possible to check the accuracy of the numerical simulations by calculating (in the frequency domain) the propagation of the RH 0% impulse through the 170 m path with RH 8%. Then given the output complex spectrum, the IFFT gives the corresponding output calculated (upper red) impulse, which is compared to the measured (lower black) impulse, under these same conditions in figure 15(a). The good agreement between the pulse shapes shows the accuracy of the simulation. The numerical simulation was also performed for the propagation of the RH 0% impulse through the 137 m long sample chamber with RH 65%. The resulting (upper red) impulse is compared to the measured (lower black) impulse under these

Table 1. Summary of Channel Simulations RH 58% and 20 °C (10 g m^{-3}).

Channel Number	Frequency (GHz)	Cycles per Bit	Bit rate (Gb s^{-1})	FWHM-BW (GHz)	Propagation Distance (m)
1	96	2	48.0	84	1000
2	144	3	48.0	96	2000
3[a]	252	3	84.0	180	100
4	342	11	31.1	60	100
5	408	13	31.4	60	110
5	408	13	31.4	60	220
5	408	13	31.4	60	440
6[a]	672	15	44.8	84	140
7[a]	852	15	56.8	108	120
7	852	12	71.0	108	100

[a] Experimentally verified with RH 65% and 21 °C (11.2 g m^{-3}) and 137 m pathlength.

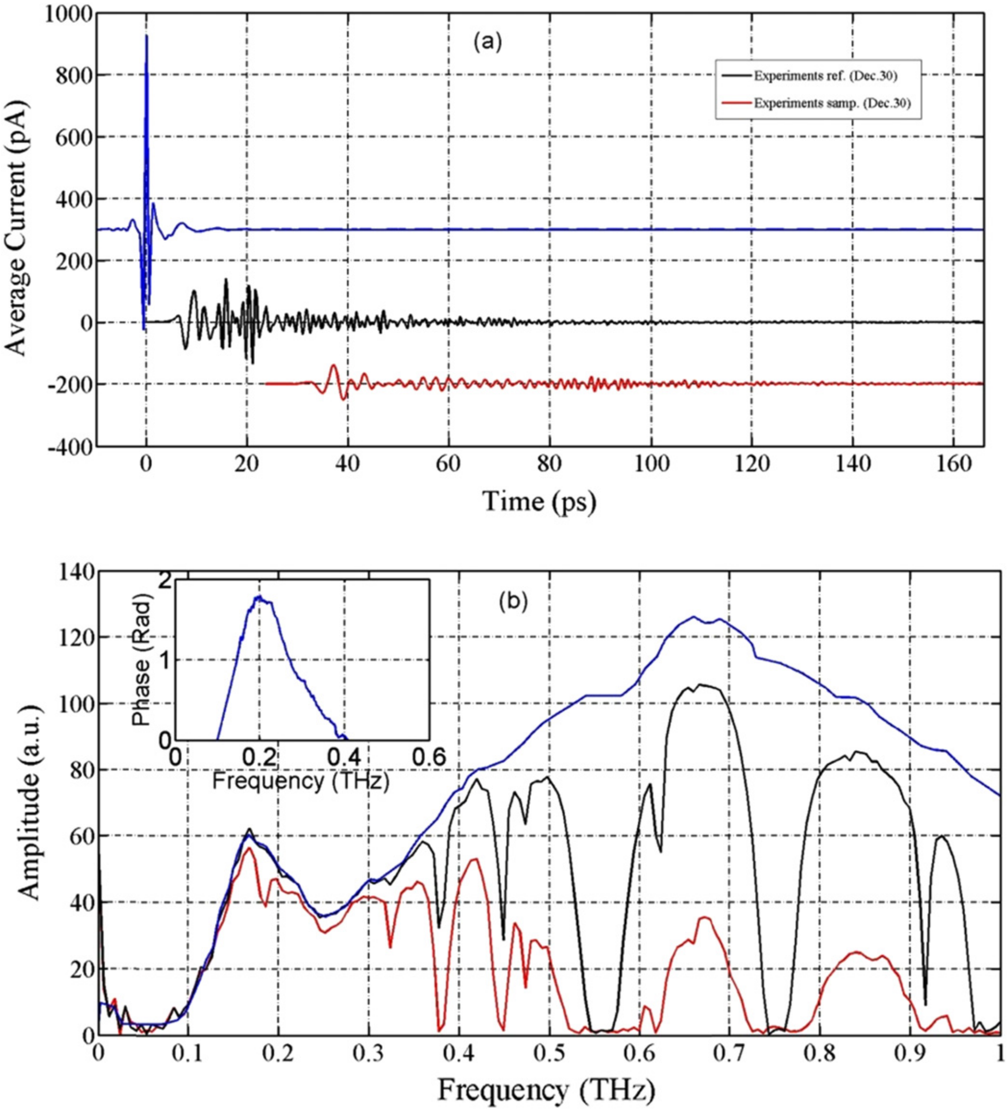

Figure 14. (a) Upper blue asymmetric RH 0% input pulse. Measured THz impulse transmitted through the 170 m path at RH 8% at 21 °C (black middle RH 8% pulse) and the THz impulse transmitted through the 137 m path sample chamber at RH 65% at 21 °C (red lower RH 65% impulse). The difference in transit times between the RH 8% and the RH 65% impulses is 27.1 ps corresponding to a change in water vapor density of $\Delta\rho = 9.8$ g m^{-3}. (b) Corresponding amplitude spectra (with no zero padding) for the RH 8% impulse (black upper spectrum), the RH 65% impulse (red lower spectrum). The top blue line spectrum shows the amplitude spectrum of the RH 0% input impulse and the insert shows the phase modulation of the RH 0% complex input spectrum.

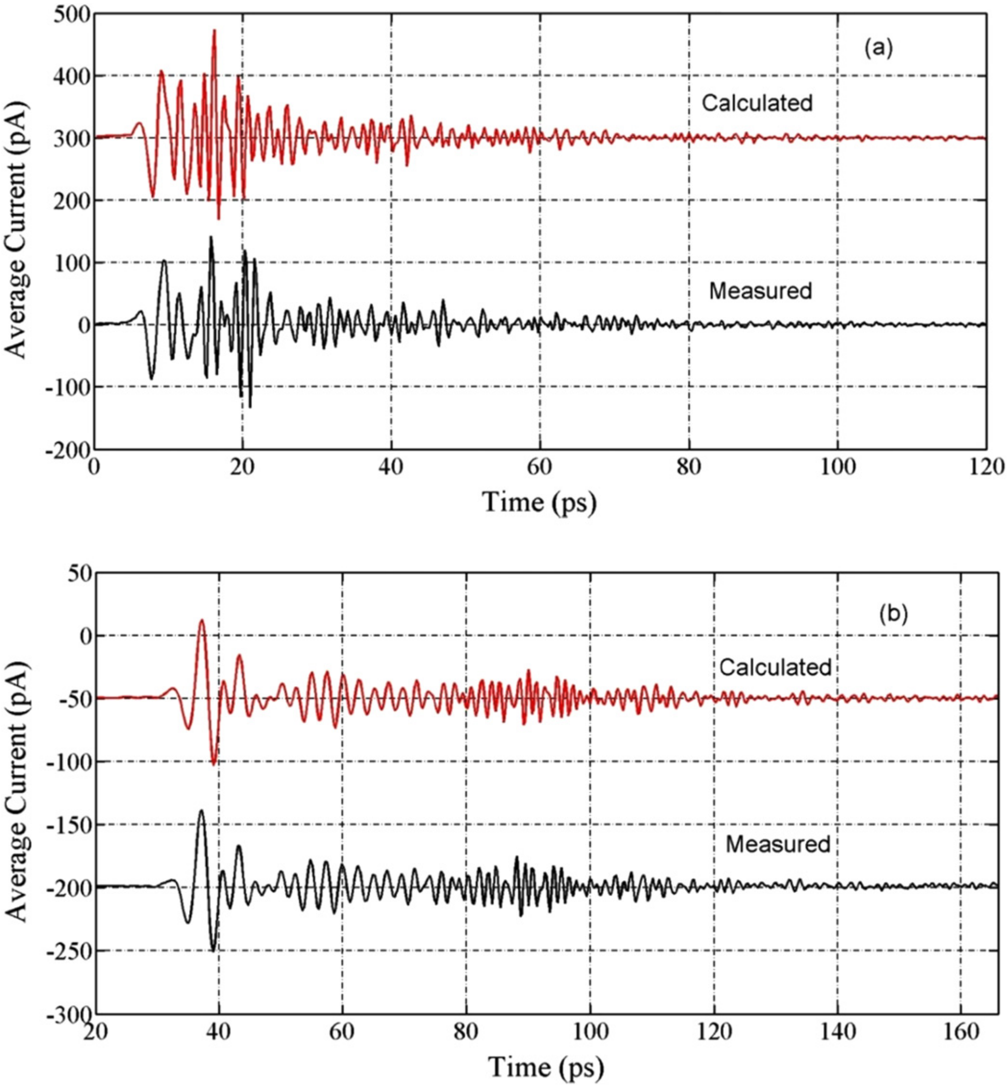

Figure 15. (a) Calculated impulse transmitted through the RH 8% (1.4 g m^{-3}) 170 m long path. The input impulse was the RH 0% reference impulse shown in figure 14(a). Measured impulse transmitted through the same RH 8%, 170 m long path. (b) Calculated impulse transmitted through an RH 65% (11.2 g m^{-3}) 137 m path in the RH-controlled sample chamber. Measured impulse transmitted through the 137 m RH 65% path.

same conditions in figure 15(b). The agreement is excellent for the two pulse shapes out to 80 ps.

For the comparison of the bit impulse simulation with the measurements In figures 14 and 15, the simulated output impulses for RH 65% are shown in figures 17–20, with the pathlength of 137 m for channels 3, 6 and 7. These impulses are compared with the corresponding measured output impulses, whose measured complex spectrum was multiplied by the indicated channel raised cosine spectral filter. The experimental output impulses are the IFFT of this result.

The following is a representation of the simple mathematics used to describe the simulation procedure to confirm the bit impulse propagation in Channels 3, 6 and 7. The phase modulated input impulse $SE_3(0,\ t)$, and the transform-limited input impulses $SE_6(0,\ t)$ and $SE_7(0,\ t)$ are given by

$$SE_3(0,\ t) = \text{IFFT of } F3(\omega)A_R(0,\ \omega), \tag{4a}$$

$$SE_6(0,\ t) = \text{IFFT of } F6(\omega)A_R(0,\ \omega), \tag{4b}$$

$$SE_7(0,\ t) = \text{IFFT of } F7(\omega)A_R(0,\ \omega). \tag{4c}$$

$A_R(0,\ \omega)$ is the RH 0% reference phase modulated spectrum shown as the upper blue line in figure 14(b), where the phase modulation is shown in the insert. The raised cosine filters [31], $F3(\omega)$, $F6(\omega)$, and $F7(\omega)$ are shown highlighted in figure 16(a), and their products with the input spectrum are shown in figure 16(b). The three channel filters have the center frequencies and FWHM bandwidths of F3-Channel 3, 252 GHz with a 180 GHz BW, F6-Channel 6, 672 GHz with 84 GHz BW, and F7-Channel 7, 852 GHz with 108 GHz BW.

The corresponding output spectra $SE_3(z, \omega)$, $SE_6(z, \omega)$, and $SE_7(z, \omega)$ are calculated by linear response theory using equation (3); IFFT of this output spectra $SE_3(z, \omega)$, $SE_6(z, \omega)$, and $SE_7(z, \omega)$ gives the corresponding simulated output impulses, shown in figures 17–20.

The measured output impulses $ME_3(z,\ t)$, $ME_6(z,\ t)$, and $ME_7(z,\ t)$ are obtained in the frequency domain by the

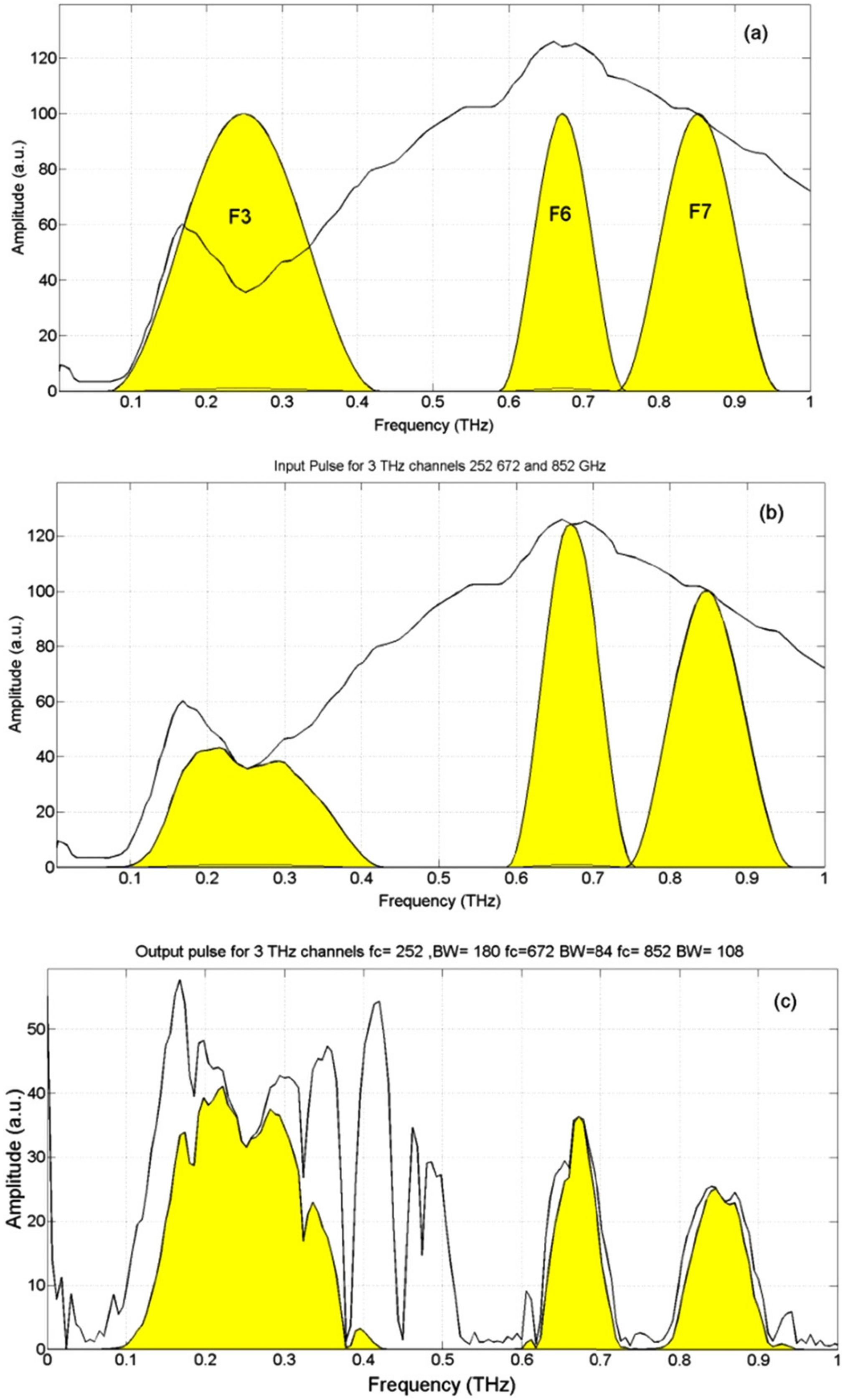

Figure 16. (a) The raised-cosine filters F3, F6, and F7 together with the RH 0% nput amplitude spectrum. The center frequency and FWHM bandwidth (BW) of the filters are F3-252 GHz-180 GHz BW, F6-672 GHz-84 GHz BW and F7-852 GHz-108 GHz BW. (b) Product of the filters and the input spectrum. (c) Product of the filters and the measured output spectrum.

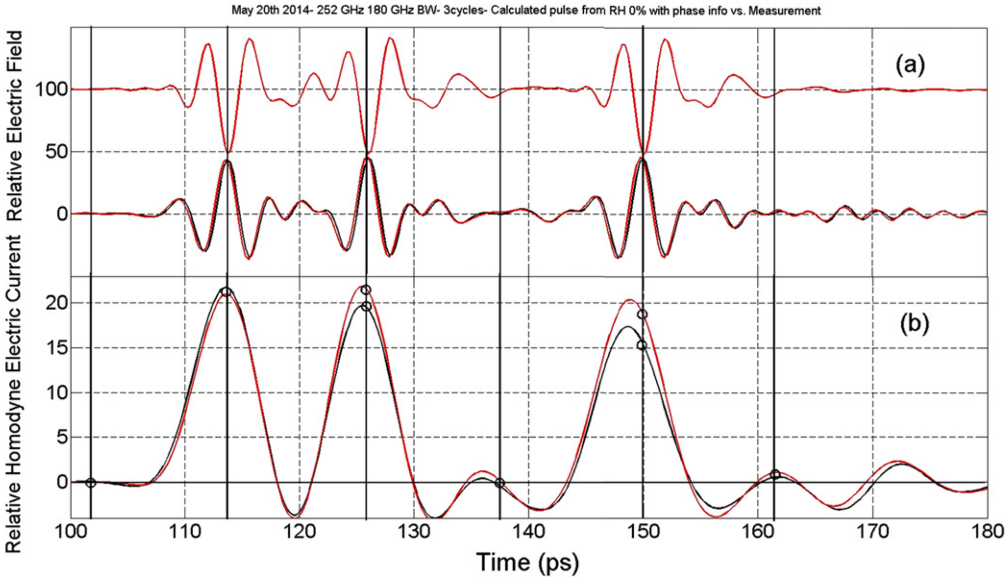

Figure 17. Comparison of experiment and theory for high bit rate propagation in **Channel 3**, 252 GHz, 84.0 Gb s^{-1}, (3 cycles), 180 GHz BW, for 137 m path propagation in the atmosphere with RH 65% (11.2 g m^{-3}) and 21 °C. (a) Upper (red) impulses are the phase modulated input impulses from the product of F3 and the RH 0% reference spectrum. Lower (red) impulses are from the simulated propagation of the input impulses. The (black) measured impulses are from the product of F3 and the RH 65% measured output spectrum. (b) Calculated homodyne output measurement (black) current pulses and the output simulated (red) current pulses, clearly showing the marked (011 010) bit sequence. Decision-point values are marked by the black circles.

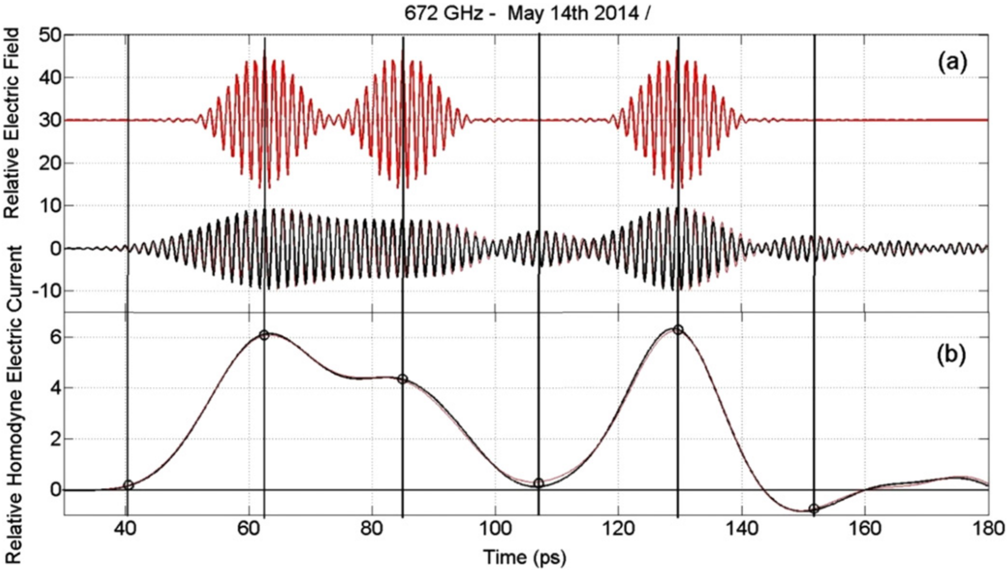

Figure 18. Comparison of experiment and theory for high bit rate propagation in **Channel** 6, 672 GHz, 44.8 Gb s^{-1}, (15 cycles), 84 GHz BW, for 137 m path propagation in the atmosphere with RH 65% (11.2 g m^{-3}) and 21 °C. (a) Upper (red) impulses (amplitudes have been divided by 4 for better display) are the coherent transform-limited input impulses from the product of F6 and the RH 0% reference spectrum. Lower (red) impulses are from the simulated propagation of the input impulses. The (black) measured impulses are from the product of F6 and the RH 65% measured output spectrum. (b) Calculated homodyne output measurement (black) current pulses and the output simulated (red) current pulses, clearly showing the marked (011 010) bit sequence. Decision-point values are marked by the black circles. Note that the agreement between the calculated and measured output pulses is so good that is difficult to distinguish the two overlapping pulses.

following simple procedure

$$\mathrm{ME}_3(\mathrm{z},\ \mathrm{t}) = \text{IFFT of } \mathrm{F3}(\omega)\mathrm{A}_\mathrm{M}(z,\ \omega) \qquad (5a)$$

$$\mathrm{ME}_6(\mathrm{z},\ \mathrm{t}) = \text{IFFT of } \mathrm{F6}(\omega)\mathrm{A}_\mathrm{M}(z,\ \omega) \qquad (5b)$$

$$\mathrm{ME}_7(\mathrm{z},\ \mathrm{t}) = \text{IFFT of } \mathrm{F7}(\omega)\mathrm{A}_\mathrm{M}(z,\ \omega). \qquad (5c)$$

$\mathrm{A}_\mathrm{M}(\mathrm{z},\ \omega)$ is the RH 65% complex output spectrum, for which the corresponding amplitude spectrum is shown in figure 14(b). The products of the filters F3(ω), F6(ω), and F7 (ω) on this spectrum are shown in figure 16(c). The corresponding output impulses are shown in figures 17–19.

For figure 17, it is important to note the improved performance of the 252 GHz, high bit rate link compared to the

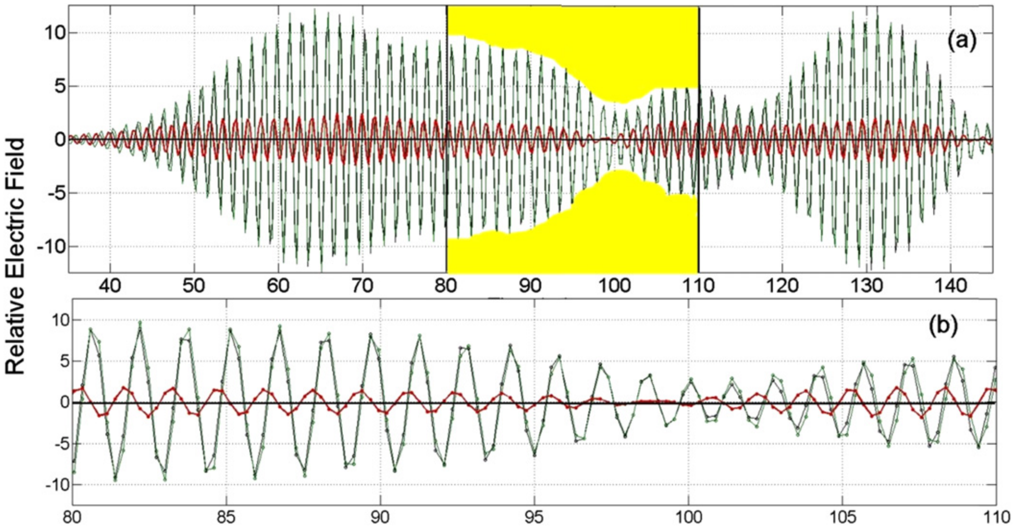

Figure 19. Comparison of experiment and theory for high bit rate propagation in **Channel 6**, 672 GHz, 44.8 Gb s^{-1}, (15 cycles), 84 GHz BW, for 137 m path propagation in the atmosphere with RH 65% (11.2 g m^{-3}) and 21 °C. (a) Measured (black) output impulses compared to the simulation (green) of figure 18(a) are shown overlapped in more detail and over a shorter time window. The residual plot between the two impulses is shown overlapped in red. (b) Measured (black) and simulated (green) and the (red) residual plot between the two impulses shown in more detail over the shortened time window from 80 to 110 ps (highlighted in yellow in figure 19(a)).

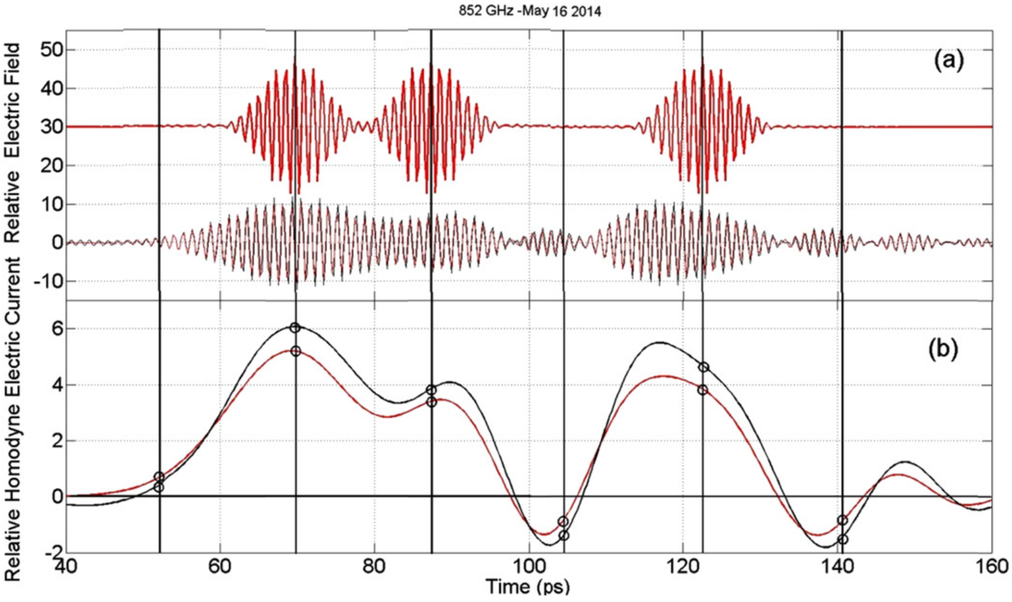

Figure 20. Comparison of experiment and theory for high bit rate propagation in **Channel 7**, 852 GHz, 56.8 Gb s^{-1}, (15 cycles), 108 GHz BW, for 137 m path propagation in the atmosphere with RH 65% (11.2 g m^{-3}) and 21 °C. (a) Upper (red) impulses (amplitudes have been divided by 4 for better display) are the coherent transform-limited input impulses from the product of F7 and the RH 0% reference spectrum. Lower (red) impulses are from the simulated propagation of the input pulses. The (black) measured impulses are from the product of F7 and the RH 65% measured output spectrum. (b) Calculated homodyne output measurement (black) upper current pulses and the output simulated (red) current pulses, clearly showing the marked (011 010) bit sequence. Decision-point values are marked by the black circles.

results shown in figure 5 for a lesser propagation length and water density. This is explained by the phase modulated experimental input impulse, which approximately cancels out the GVD phase shift for a propagation distance of 137 m. This is a relatively well-known dispersion compensation effect [31]. The agreement between the simulation and the measurement of the propagated 3 impulses is excellent. The slight difference is a simple relative time shift.

For Channel 6, as shown in figure 18(a), the agreement between simulation and measurement of the propagated 3 impulses is excellent. This is shown in the complete overlap of theory and measurement in figure 18(a). This overlap is shown in more detail in figure 19, where the peaks and minimums of the two oscillations are in synchronization and have nearly the same amplitude. The residual plot between the two is much smaller and is out of phase by $\pi/2$. The residual zeros occur at the maximum and minimum of the two oscillations with the maximums near the crossing points. This excellent agreement confirms the accuracy of the simulations.

Summary

For the first time we have simulated dispersion-limited high bit rate impulse propagation through the atmosphere for the seven communication channels within the corresponding atmospheric windows. The dispersion-limited results are important for robust THz links and for the assessment of longer path propagation possibilities of the more complex digital data transmission of the more complicated amplitude and phase modulations of QPSK, 8QAM and 16QAM in the data carrier frequency, which has been recently demonstrated.

We have shown that the seven communication channels have the return-to-zero impulse modulated high bit rate properties: **Channel 1**, at 96 GHz, Bandwidth (BW) 84 GHz, 48 Gb s^{-1} for 1000 m; **Channel 2**, at 144 GHz, BW 96 GHz, 48.0 Gb s^{-1} for 2000 m; **Channel 3**, at 252 GHz, BW 180 GHz, 84.0 Gb s^{-1} for 100 m; **Channel 4**, at 342 GHz, BW 60 GHz, 31.1 Gb s^{-1} for 100 m; **Channel 5**, at 408 GHz, BW 60 GHz, 31.4 Gb s^{-1} for 110 m, 220 m, and 440 m; **Channel 6**, at 672 GHz, BW 84 GHz, 44.8 Gb s^{-1} for 140 m; and **Channel 7**, at 852 GHz, BW 108 GHz, 56.8 Gb s^{-1} for 120 m, and with 71.0 Gb s^{-1} for 100 m.

For the first time, the high bit rate results for Channels 3, 6, and 7 were experimentally confirmed for the simulations with a propagation pathlength of 137 m and RH 65% (11.2 g m^{-3}). Excellent agreement between measurement and theory was obtained for **Channel 3** at 252 GHz, bit rate 84 Gb s^{-1}, FWHM bandwidth BW 180 GHz; **Channel 6** at 672 GHz, 45 Gb s^{-1}, BW 84 GHz; and **Channel 7** at 852 GHz, 57 Gb s^{-1}, BW 108 GHz, thereby showing the high bit rate potential of impulse modulated THz links. This excellent agreement also shows the possibility of accurately simulating the longer-path potential for the ultra-high bit rate propagation of the more complex phase and amplitude modulated QPSK, 8QAM, and 16QAM digital data.

Acknowledgment

This work was partially supported by the National Science Foundation.

References

[1] Deepak A, Wilkerson T D and Ruhnke L H (ed) 1980 Atmospheric water vapor *Proc. Int. Workshop Atmospheric Water Vapor* (Vail, Colorado, September 11–13, 1979) (New York: Academic Press)

[2] Burch D E and Gryvnak D A 1980 Continuum absorption by water vapor in the infrared and millimeter regions *Atmospheric Water Vapor* ed A Deepak pp 47–76 *Proc. of the Int. Workshop on Atmospheric Water Vapor* (Vail, Colorado, September 11–13, 1979) (New York: Academic Press)

[3] Siegel P H 2002 Terahertz technology *IEEE Trans. Microwave Theory Tech.* **50** 910–28

[4] Appleby R and Wallace H B 2007 Standoff detection of weapons and contraband in the 100 GHz to 1 THz region *IEEE Trans. Antennas Propag.* **55** 2944–56

[5] Yang Y, Shutler A and Grischkowsky D 2011 Measurement of the transmission of the atmosphere from 0.2 to 2 THz *Opt. Express* **19** 8830–8

[6] Yang Y, Mandehgar M and Grischkowsky D 2012 Understanding THz pulse transmission in the atmosphere *IEEE Trans. THz Sci. Technol.* **2** 406–15

[7] Van Vleck J H and Weisskopf V F 1945 On the shape of collision-broadened lines *Rev. Mod. Phys.* **17** 227–36

[8] Van Vleck J H 1947 The absorption of microwaves by oxygen *Phys. Rev.* **71** 413–24

[9] Pickett H M, Poynter R L, Cohen E A, Delitsky M L, Pearson J C and Muller H S P 1998 Sub-millimeter, millimeter, and microwave spectral line catalog *JQSRT* **60** 883–90 (Access to specific catalog entries may be found at http://spec.jpl.nasa.gov/)

[10] Rothman L S *et al* 2009 The HITRAN 2008 molecular spectroscopic database *JQSRT* **110** 533–72

[11] Piesiewicz R, Kleine-Ostmann T, Krumbholz N, Mittleman D, Koch M, Schoebel J and Kurner T 2007 Short-range ultra-broadband terahertz communications: concepts and perspectives *IEEE Antennas Propag. Mag.* **49** 24–39

[12] Wells J 2009 Faster than fiber: the future of multi-Gb s^{-1} wireless *IEEE Microwave Magazine* **10** 104–12

[13] Kosugi T, Hirata A, Nagatsuma T and Kado Y 2009 MM-wave long-range wireless systems *IEEE Microwave Magazine* **10** 68–76

[14] Federici J and Moeller L 2010 Review of terahertz and subterahertz wireless communications *J. Appl. Phys.* **107** 111101

[15] Cianca E, Rossi T, Yaholom A, Pinhasi Y, Farserotu J and Sacchi C 2011 EHF for satellite communications: the new broadband frontier *Proc. of the IEEE* **99** 1858–81

[16] Kleine-Ostmann T and Nagatsuma T 2011 A review on terahertz communications research *J. Infrared Milli Terahz Waves* **32** 143–71

[17] Mandehgar M, Yang Y and Grischkowsky D 2013 Atmosphere characterization for simulation of the two optimal wireless THz digital communication links *Opt. Lett.* **38** 3437–40

[18] Yang Y, Mandehgar M and Grischkowsky D 2014 THz-TDS characterization of the digital communication channels of the atmosphere *J. Infrared, Millimeter Terahertz Waves* at press doi:10.1007/S10762-014-0099-3

[19] Yang Y, Mandehgar M and Grischkowsky D 2014 Determination of the water vapor continuum absorption by THz-TDS and molecular response theory *Optics Express* **22** 4388–403

[20] Vlasov Y A 2012 Silicon CMOS-integrated nano-photonics for computer and data communications beyond 100 G *IEEE Commun. Mag.* **50** 567–72

[21] Moeller L, Federici J and Su K 2011 THz wireless communications: 2.5 Gb s^{-1} error-free transmission at 625 GHz using a narrow-bandwidth 1 mW THz source *30th URSI General Assembly and Scientific Symposium (URSI GASS),* 4 (electronic) *(Istanbul)*

[22] Kallfass I, Antes J, Lopez-Diaz D, Wagner S, Tessmann A and Leuther A 2012 Broadband active integrated circuits for terahertz communication *Proc. of 18th European Wireless Conf. European Wireless* EW pp 1–5

[23] Song H-J, Ajito K, Muramoto Y, Wakatsuki A, Nagatsuma T and Kukutsu N 2012 24 Gbit s^{-1} data transmission in 300 GHz band for future terahertz communications *IET Electron. Lett.* **48** 953–4

[24] Koenig S *et al* 2013 Wireless sub-THz communication system with high data rate *Nat. Photonics* **7** 977–81

[25] Nagatsuma T, Horiguchi S, Minamikata Y, Yoshimizu Y, Hisatake S, Kuwano S, Yoshimoto N, Terada J and Takahashi H 2013 Terahertz wireless communications based on photonics technologies *Opt. Express* **21** 23736–47

[26] Ducournau G, Szriftgiser P, Beck A, Bacquet D, Pavanello F, Peytavit E, Zaknoune M, Akalin T and Lampin J-F 2014 Ultrawide-bandwidth single-channel 0.4 THz wireless link combining broadband Quasi-optic photomixer and coherent detection *IEEE Trans. on THz Science and Tech.* **4** 328–37

[27] Scholtz R A 1993 Multiple access with time hopping impulse modulation *Proc. MILCOM93* (Bedford, MA)

[28] Win M Z and Scholtz R A 1998 Impulse radio: how it works *IEEE Comm. Lett.* **2** 10–2

[29] Nakasha Y, Sato M, Tajima T, Kawano Y, Suzuki T, Takahashi T, Makiyama K, Ohki T and Hara N 2009 W-band transmitter and receiver modules for 10 Gb s^{-1} impulse radio *Dig. IEEE MTT-S Intern. Microwave Symp. Digest* pp 553–6

[30] Hayashi H, Nakasha Y, Aota M and Sato N 2013 Millimeter-wave impulse radio technology *Fujitsu Sci. Tech. J.* **49** 350–5

[31] Agrawal G P 2002 *Fiber-Optic Communication Systems* 3rd edn (New York: Wiley)

[32] Yang Y, Mandehgar M and Grischkowsky D 2011 Broad-band THz pulse transmission through the atmosphere *IEEE Trans. THz Sci. Technol.* **1** 264–73

[33] Yang Y, Mandehgar M and Grischkowsky D 2012 Time domain measurement of the THz refractivity of water vapor *Opt. Express* **20** 26208–18